Scalable, Time-of-Flight and Depth-of-Interaction Detector Units for High-Resolution PET Systems

Vanessa Nadig, *Member, IEEE*, Stefan Gundacker, *Member, IEEE*, David Schug,
Katrin Herweg, *Graduate Student Member, IEEE*, Konstantin Weindel, Harald Radermacher,
Florian Mueller, *Member, IEEE* Bjoern Weissler, and Volkmar Schulz, *Senior Member, IEEE*

Abstract—Resolving the depth of interaction (DOI) of a γ-photon in the scintillator is necessary to correct for parallax errors in organ-dedicated and large-scale time-of-flight positron emission tomography (TOF-PET) scanners or enable the precise recovery of Compton-scattered γ-photons. Doubling the number of readout channels and moving toward more complex detector designs are methods to encode DOI, often associated with high costs. We propose a DOI-capable TOF-PET detector unit concept confining light-sharing to two detector channels, where the high benefit lies in scalability and the prospect of Compton recovery between adjacent units. We evaluate these scalable, DOI-capable unit concepts, realizing DOI encoding between two LYSO:Ce,Ca crystals ($3 \times 3 \times 20$ mm^3; Taiwan Applied Crystals) one-to-one coupled to two Broadcom AFBR-S4N33C013 silicon-photomultipliers (SiPMs) read out with the TOFPET2 ASIC. The best-performing unit employing a triangular reflector sheet and optical glue between the two crystals and mounted on two FBK NUV-MT SiPMs results in a DOI resolution of about 3 mm (RMSE) based on the energy ratio digitized by the two channels while maintaining a coincidence time resolution (CTR) of 226 ps (FWHM) with TOFPET2 ASIC readout, applying a linear DOI correction. Using HF readout, the CTR of the proposed detector unit was improved to 141 ps (FWHM).

Index Terms—Data correction techniques, DOI, electronics, HF readout, pre-clinical imaging systems, PET, photodetector technology, radiation detectors for medical applications, scintillators, signal processing, TOF, TOFPET2 ASIC.

I. INTRODUCTION

WHILE currently applied for mid- to late-stage disease diagnostics, organ-dedicated positron emission tomography (PET) is envisioned to become a future diagnosis tool to detect, classify and treat early stage neurological and inflammatory diseases, such as Alzheimer's and Parkinson's among the population. Before undergoing a PET scan, patients are injected with a tracer sensitive to β-amyloid aggregations in case of Alzheimer's [1], [2]. Upon decay, these tracers emit positrons, which recombine with electrons in the surrounding tissue, releasing two 511-keV γ-photons back to back. These are commonly stopped and digitized by detector blocks, which enclose the patient and consist of dense scintillation material, a photosensor and customized readout electronics [3]. For a fast, reliable and—most of all—safe screening process, a high-signal-to-noise ratio (SNR) and a high sensitivity are required to reduce scan times and administered dosage for patients as much as possible [4], [5], [6], [7]. Achieving a high SNR in a PET image is directly linked to a high time-of-flight (TOF) coincidence time resolution (CTR), where the gain in SNR compared to a non-TOF image can be described as reported in [8], [9], and [10] via

$$\frac{\text{SNR}_{\text{TOF}}}{\text{SNR}_{\text{non}-\text{TOF}}} \propto \sqrt{\frac{D}{\frac{c_0}{2} \cdot \text{CTR}}} \tag{1}$$

for an object of the diameter D and the 511-keV γ-photons traveling with the speed of light in vacuum c_0. To boost the sensitivity of a PET system, apart from employing dense scintillation materials with a high-atomic number Z [11], [12], the PET detectors can be moved closer to the organ of interest (e.g. for brain PET) [13], [14] or the solid-angle coverage can be increased by scaling the aFOV to several meters (total-body PET) [15], [16], [17], [18], [19]. However, this approach results in so-called parallax errors (see Fig. 1), i.e., positioning errors that are attributed to an unknown depth of interaction (DOI) of the γ-photon inside the scintillator. Parallax errors occur despite a high CTR and a precise location of the event along the line of response (LOR) [20]. About five years ago, without aiming at encoding DOI, state-of-the-art TOF-PET systems realized a CTR of 214 ps [21], which until today is the point of reference for the timing performance of newly developed commercial systems is compared to. A preclinical system compatible with magnetic resonance imaging (MRI) achieved a similar performance [22]. Knowing that each element of the detection chain, i.e., the scintillator, the photosensor and the readout electronics, contribute
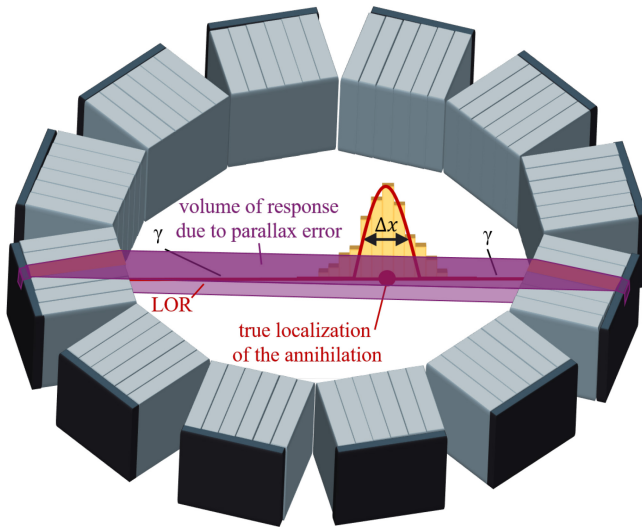
Fig. 1. Schematic representation of a PET gantry without correction for DOI. The annihilation point along the LOR is reconstructed with the precision of the TOF kernel Δx. However, its position is smeared across the region of interest depending on the DOI assumed, which is called parallax error.

to the achievable CTR [23], [24], efforts have been concentrated on optimizing each component and have shown to push the CTR to new limits [25], [26], [27], [28]. Recently, bench-top experiments have realized sub-100 ps CTR with commercially available Ca- and Ce-doped lutetium yttrium oxyorthosilicate (LYSO:Ce,Ca; $3 \times 3 \times 20\,mm^3$) crystals and novel silicon-photomultipliers (SiPMs) employing a metal-in-trench (MT) technology (Broadcom NUV-MT; $3.8 \times 3.8\,mm^2$, 40-μm SPADs), which have been read out by advanced high-frequency (HF) electronics [29]. Similar performance has been achieved using smaller ($3 \times 3 \times 10\,mm^3$) fast LGSO crystals and SiPMs from SensL [30].

In parallel to advances in timing performance, a multitude of concepts to encode the DOI of a γ-photon has been developed [20], [31] throughout the past decades, evoking many patents [32], [33], [34], [35]. For example, concepts considered multilayered scintillator or detector matrices [36], [37], [38], [39] and different reflector geometries in one-to-one coupled matrices [40], [41], [42] or other light-sharing concepts [14], [43]. Other approaches involved (semi-)monolithic geometries for multiple channels [44], [45], [46], [47], [48] and double-sided readout for single scintillator bins [49], [50], [51], [52]. Most of these attempts focus on precise DOI resolution rather than maintaining ultrafast timing capabilities. So far, these attempts have yet to exploit the combination of recent fast-timing developments, including co-doped scintillation material, novel photosensor techniques, and proposed HF readout concepts.

We aim to develop scalable TOF- and DOI-capable detector units with the ultimate goal of achieving a CTR of 100 ps in a detector matrix - also by means of correcting timestamps for the DOI and related influences on the optical photons' transfer time. By confining light-sharing to only two channels, this unit approach requires minimal changes to the actual manufacturing and assembly process of a PET detector matrix and is likely to maintain excellent TOF resolution. Additionally, it provides scalability for any given matrix geometry and does

not necessarily require an out-of-system calibration of the chosen DOI-encoding variable.

In this study, as the first step, different DOI concepts will be presented to provide a broad comparison of their DOI and CTR capabilities using the same photosensor technology and optimized electronic readout, which is currently lacking in the literature. Here, a separability in two to four DOI bins is anticipated to be beneficial with the prospect of an SNR improvement in clinical systems. For the second step, the most promising TOF-DOI unit concept will be evaluated, focussing on its TOF and DOI capabilities with novel NUV-MT SiPMs.

II. MATERIALS

The following paragraphs provide details on the TOF-DOI unit design and readout. The ^{22}Na source used in all experiments had an activity of 2.5 MBq. The setup was placed in a dark chamber regulated to 16 °C ambient temperature.

A. Reference Detector

For all conducted experiments, we employed a Broadcom AFBR-S4N33C013 SiPM coupled to a small-size LYSO:Ce crystal ($2 \times 2 \times 3\,mm^3$; Epic-crystal) using Cargille Meltmount™ as reference detector.

B. TOF-DOI Unit Design

As depicted in Fig. 2, we coupled two LYSO:Ce,Ca crystals ($3 \times 3 \times 20\,mm^3$, Taiwan Applied Crystal (TAC)) one-to-one to two Broadcom AFBR-S4N33C013 SiPMs ($3 \times 3\,mm^2$, 30-μm SPADs, breakdown voltage 26.5 V) using Cargille Meltmount™ ($n = 1.582$). Different concepts to continuously encode DOI were implemented between the two crystals (C0, C1), including reflector slices (ESR-OCA-ESR; 155 -μm thickness), depolishing (DP), and carvings of 1 mm depth of the crystal faces (c.f. Figs. 3 and 4). All units were wrapped in Teflon tape. For the unit concept with a triangular ESR sheet and Meltmount™, different coatings (glued ESR, TiO$_2$ coating) were tested in comparison to Teflon wrapping to examine the effect of matrix-applicable coating techniques.

With recent technological advances, SiPMs employing the novel MT technology have become available, which are characterized by reduced internal crosstalk and a higher photon detection efficiency (PDE) due to operability at higher overvoltages [29], [54]. To provide a benchmark for the TOF and DOI resolution achieved with this technology, the most promising TOF-DOI unit concept was additionally evaluated with NUV-MT SiPMs ($3 \times 3\,mm^2$, 40-μm SPADs) fabricated by Fondazione Bruno Kessler (FBK). The breakdown voltage of these SiPMs is 32.5 V.

A pole-zero cancelation circuit (100 pF, 390 Ω) was implemented on the sensor board to reduce baseline shifts [53] before routing the signal into the input stage of the TOFPET2 ASIC by PETsys Electronics S.A. (version 2c) [55] or HF readout electronics, which were adapted from Krake et al.[25] and Gundacker et al. [26].
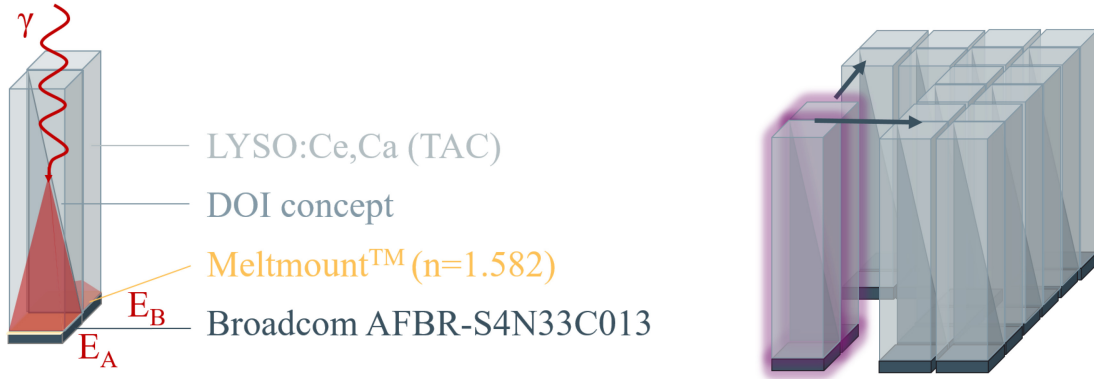
Fig. 2. Design concept of the investigated TOF-DOI detector units. A unit consists of two analog SiPMs coupled to two LYSO:Ce,Ca crystals (left), which can be scaled to any desired matrix geometry, e.g., a four-by-four pixel matrix (right).
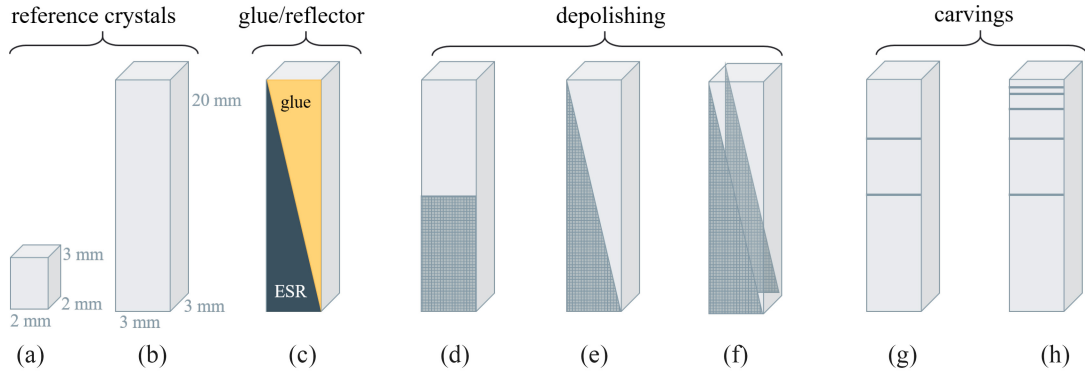

Fig. 3. Schematic drawing of the different DOI concepts investigated in this study. All crystal pixels were cut out of LYSO:Ce,Ca ingots and manufactured at Taiwan Applied Crystal Co. Ltd. In addition to reference crystals with sizes $2 \times 2 \times 3\,\mathrm{mm}^3$ (a) and $3 \times 3 \times 20\,\mathrm{mm}^3$ (b) and reflectors and glue layers mounted by the authors (c). The manufacturer realized the depolished rectangular (d) and triangular (e) and (f) crystal faces and carvings at different heights and of 1-mm depth (g) and (h).
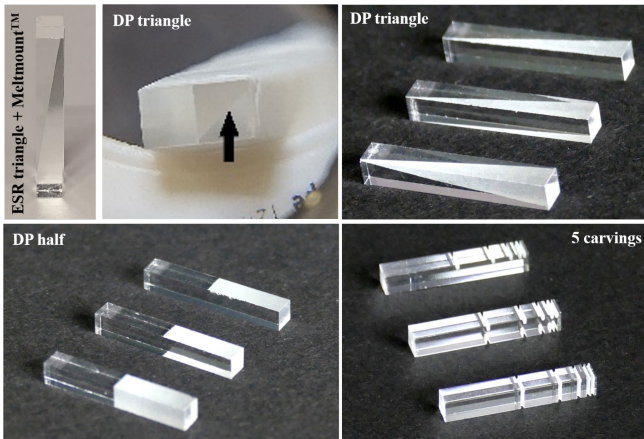

Fig. 4. Pictures taken during TOF-DOI unit assembly. The depicted units show triangular and carved DOI concepts as in Fig. 3(c), (d)–(f), and (h).

C. TOF-DOI Unit Readout

For evaluation with a system-applicable and commercially available readout, each unit was connected to the TOFPET2 ASIC via a custom-designed adapter board (see Fig. 5(b)). The TOFPET2 ASIC was operated with default trigger configuration, but with a reduced input stage impedance ($R_{\mathrm{in}} = 11\,\Omega$, fe_ib1 = 0). The trigger thresholds were kept constant at vth_t1 = 20 (disc_lsb_t1 = 55), vth_t2 = 20 and

vth_e = 15. The signal energy was digitized using a charge-integration method. To assess the limits in TOF performance via HF readout, a circuit board housing two channels of the power-efficient HF electronics from Krake et al. [25] was developed (c.f. Fig. 5(a)). Afterward, a small mezzanine board is used to combine the fast timing and energy channel [56] before the signals are digitized via a Lecroy Waverunner 9404M-MS (bandwidth 4 GHz, 20 GS s^{-1}). To find the optimum operation point, bias scans were performed with both readout electronics in a range of 4 to 8-V overvoltage with the TOFPET2 ASIC and in a range of 6 to 11.5-V overvoltage with the HF readout electronics for Broadcom AFBR-S4N33C013 SiPMs. For the FBK NUV-MT SiPMs, these ranges were adapted to a range of 4 to 15-V overvoltage with the TOFPET2 ASIC and in a range of 4.5 to 12.5-V overvoltage with the HF readout electronics.

III. METHODS

The following paragraphs provide details on the experimental setups, data acquisition and processing methods applied in this study.

A. Reference Detector

The CTR of the reference detector was characterized by coincidence measurements with two identical detectors. In all
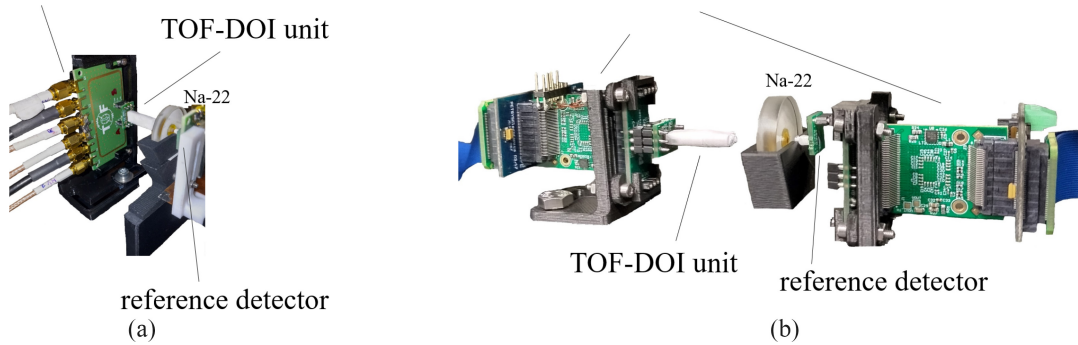
Fig. 5.   Coincidence setups employing ultrafast HF electronics adapted from Krake et al. [25] to enable the readout of two adjacent detector channels via an oscilloscope (a) and the TOFPET2 ASIC evaluation kit with custom-designed sensor boards, employing a pole-zero filter circuit [53] (b).

following experiments, the obtained value CTR_{meas} is then corrected for the CTR of the reference CTR_{ref} using

$$CTR_{unit} = \sqrt{2 \cdot CTR_{meas}^2 - CTR_{ref}^2} \qquad (2)$$

with CTR_{unit} being reported as the CTR of the TOF-DOI unit.

B. Event Processing

Events registered in the detector unit are clustered within a period of 15 ns. Only clusters with both channel values digitized are accepted. For each event, the crystal stopping the incident γ-photon (C0, C1) is identified via the sensor channel (A, B) digitizing the higher raw energy value (main channel; c.f. Fig. 6). For each crystal, energy histograms of the main channel and adjacent channel are considered for processing. The event timestamp assigned is the timestamp of the main channel. The energy ratio

$$\varepsilon = \frac{E_A - E_B}{E_A + E_B} \qquad (3)$$

of the raw energy values E_A and E_B was computed as a DOI-encoding variable (similar to concepts shown in [31]).

C. Coincidence Experiments at Different Depths of Interaction Using Collimated Radiation

1) Setup and DOI-Encoding Variable: The setup was arranged to collimate the activity of the source (c.f. Fig. 7(a); source diameter 0.5 mm, total computed beam width 1.0 mm). The position of the crystal ends was calibrated by shifting the TOF-DOI unit with respect to the position of the source and reference detector using a translation stage. A fine step size of 125 μm, i.e., 50 motor steps à 2.5 μm calibrated via linear regression, was used to acquire the coincidence rate as a function of the position along the DOI axis (c.f. Fig. 8(a)) with the purpose to assess the width of the collimated beam. The TOFPET2 ASIC is operated using its hardware coincidence trigger and the acquired coincidence rate is plotted against the position of the translation stage. After computing the rolling average of the acquired coincidences and differential coincidence rate, two Gaussians are fitted to the peaks, indicating a rapid rate increase and decrease (c.f. Fig. 8(b)), respectively, corresponding to the ends of the crystal [57].

After identifying the position of the crystal ends, a scan at different DOI was performed with a pitch of 2 mm (larger than
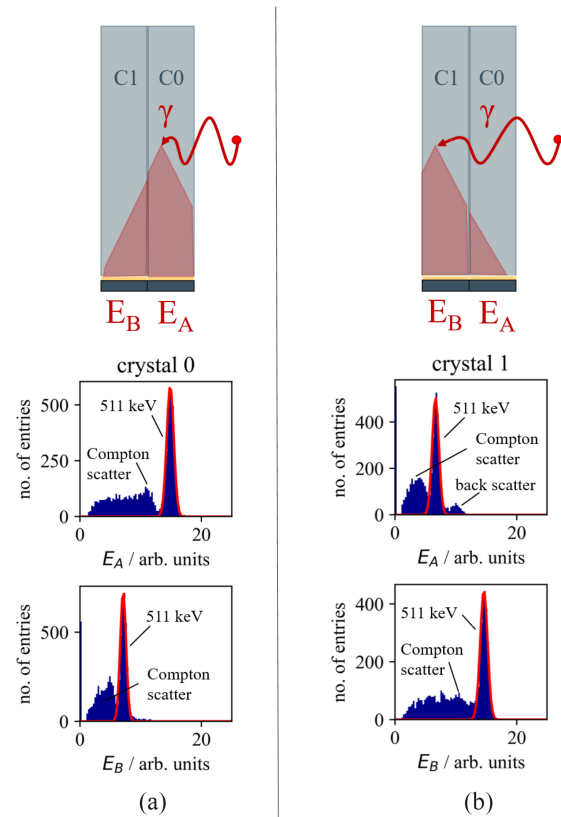
Fig. 6.   Coincident raw energy value spectra acquired via the TOFPET2 ASIC for γ-photons stopped in crystal C0 and C1, respectively, each displaying the photopeak corresponding to 511 keV events and the Compton continuum. (a) Raw energy value spectra in channels A and B for γ-photons stopped in crystal C0. Channel A is the main channel registering a higher amount of energy. (b) Raw energy value spectra in channels A and B for γ-photons stopped in crystal C1. Channel B is the main channel, registering a higher amount of energy. Channel A displays a distinctive backscatter peak.

the beam width), which resulted in nine irradiation positions measured for 900 s, excluding the ones located precisely at the crystal ends. This way about 11 000 coincidences are acquired per irradiated position.

2) Analytical Models for DOI Encoding: We selected coincident events within a $\pm 2\sigma$-environment of the photopeak in the main and adjacent channel spectrum of each of the crystals identified via the highest raw energy value to reject intercrystal scatter between the two crystals of the DOI unit. A shift

Fig. 7. Sketch of both coincidence setups used: electronic collimation of the radiation to investigate performance parameters depending on the DOI (a) and head-on irradiation of a TOF-DOI unit (b).

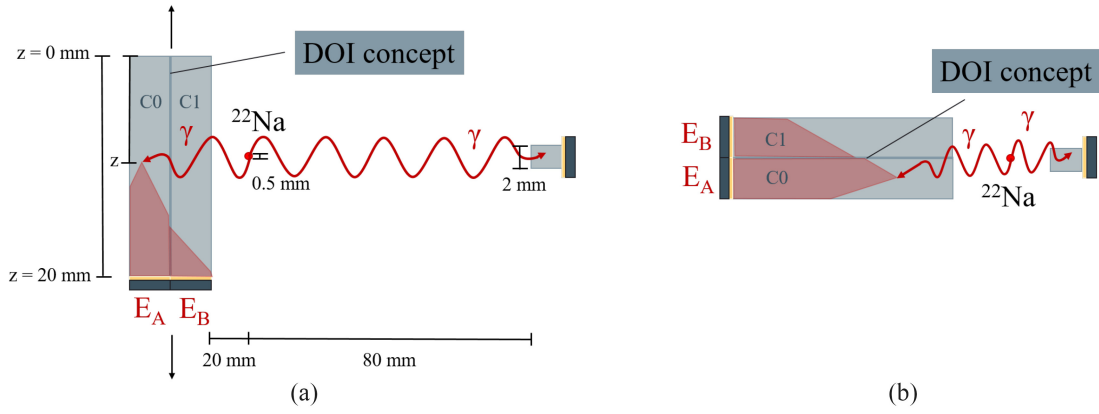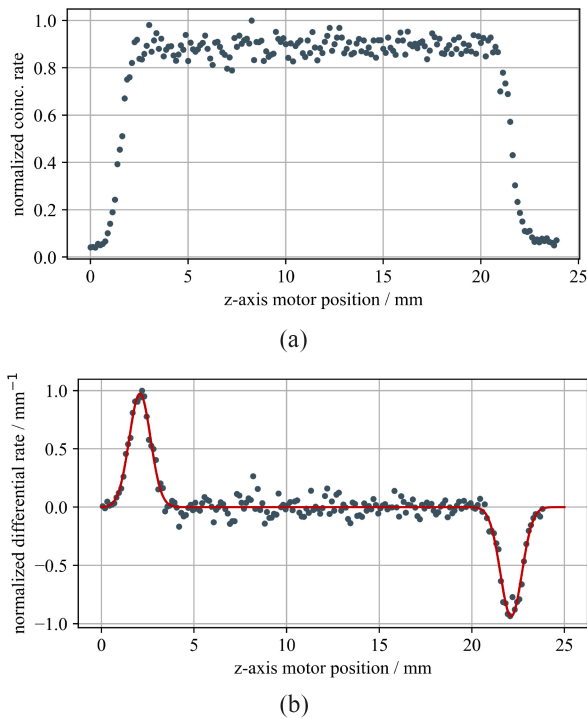Fig. 8. Characterization of the collimated beam. (a) Normalized coincidence rate acquired for positions along the motor axis with a step width of 125 µm. (b) Normalized differential rate. The two peaks indicate the crystal ends. The FWHM of the peaks can be taken as a measure for the width of the beam and was determined to 1.4 mm.

of the ratio ε with the irradiated DOI position is observed for both crystals of each assembled detector unit. We fit Gaussians to the ε-histograms (c.f. Fig. 9(a)) and plot the Gaussian centroids of the ε-histograms against the DOI coordinate z, which displays an S-curve (c.f. Fig. 9(b)). Therefore, to establish a conversion method between ε and z, a sigmoid function

$$\varepsilon(z) = \frac{A}{1 + e^{-k \cdot (z - z_0)}} + b \qquad (4)$$

with the amplitude A and offset b is fit to the means of the ε-distribution at each calibration position. Its inverse function then assigns a DOI coordinate to a given energy ratio ε.

For a TOF-DOI unit concept with two crystals, which feature six polished faces (c.f. Fig. 3(b)), the orientation of the S-curve changes compared to the other DOI concepts. Hence, the conversion method had to be changed to a third-order polynomial fit

$$\varepsilon(z) = C \cdot \left(z - \frac{l}{2}\right)^3 + d \qquad (5)$$

with the amplitude C and offset d to match the behavior of the light-sharing between the two unit channels. The variable l denotes the length of the crystal pixel. The model can be simplified by neglecting edge effects, i.e., a saturation of the DOI-encoding variable ε toward the top and bottom face of the crystals. A linear model

$$\varepsilon(z) = m \cdot z + n$$

with a slope m and a y-axis intercept n is fitted to the data, only including DOI positions between 4 and 16 mm. For all models, events which are positioned at DOIs $z > 20$ mm and $z < 0$ mm were truncated and positioned at $z = 20$ mm and $z = 0$ mm, respectively.

3) DOI Resolution: Using the same data set and all irradiated DOI positions, including the crystal ends, the point spread function (PSF) of the computed DOI versus the true DOI is plotted as a 1-D histogram for selected DOIs (c.f. Fig. 9(c)) or in a 2-D histogram (c.f. Fig. 10(a) and (b)) to check the performance of both models. We condense the PSF at each labeled position into five scalar performance values. The mean absolute error (MAE) in positioning is computed as the mean of the absolute value of the difference between true DOI and computed DOI and plotted as a function of the true DOI (c.f. Fig. 10(c)). Furthermore, the bias in positioning, i.e., the shift of the mean of the distribution of the computed DOIs with respect to the true DOI (c.f. Fig. 10(d)), and the percentile distance r50 and r90 of positioning the events correctly (c.f. Fig. 10(e)) are computed, which is the value of the radius around the true position that encloses 50 % and 90 % of the events to probe the PSF in the central region and the tail region. By being centered on the labeled position, these values are sensitive to the bias in positioning. Corresponding
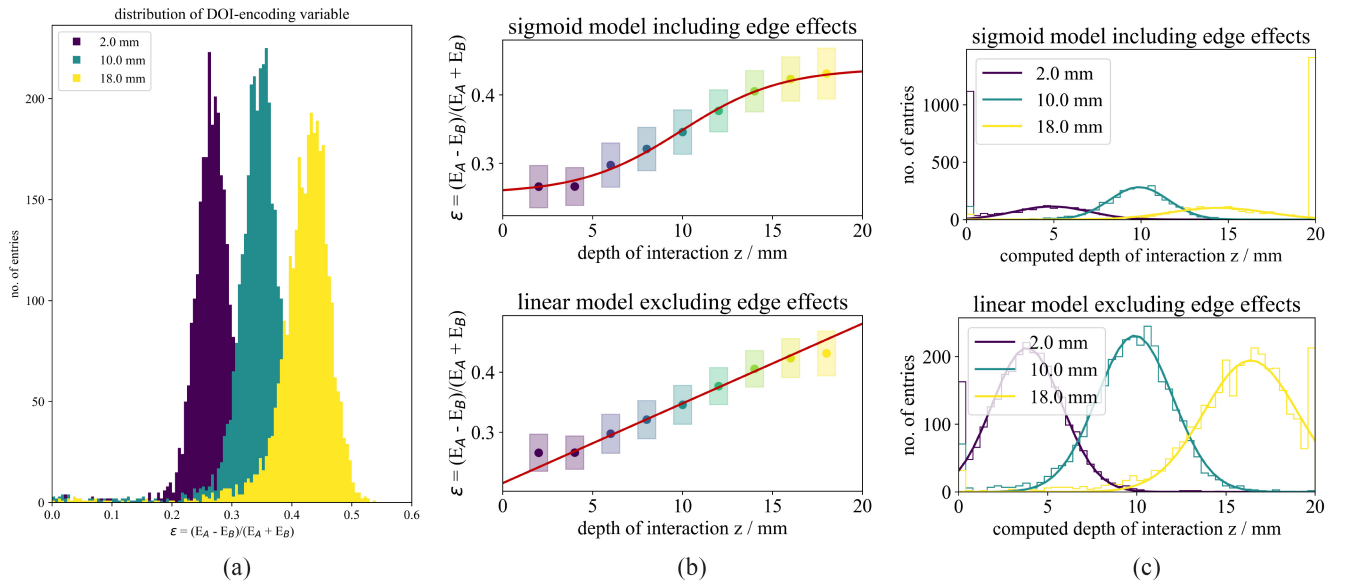
Fig. 9.   Histograms of the DOI-encoding variable ε at different DOI (a) and change of the DOI-encoding ε variable over the DOI (b). Graphs are shown for the example of a triangular reflector sheet [c.f. Fig. 3(c)] and TiO_2 coating and events filtered to $\pm 2\sigma$ around the photopeak of the raw energy spectrum of the main channel and $\pm 2\sigma$ around the light-sharing peak of the raw energy spectrum of the adjacent channel. The boxes plotted are the FWHM of the Gaussian fit to the distribution of the variable at a given DOI. The distribution of the computed DOI is shown in (c) at different DOI labels.

to a coarser representation of the PSF in Fig. 10(a), the crystal is divided into bins of 5 mm and 10 mm and a confusion matrix of the true DOI versus the computed DOI is plotted. A DOI resolution can be computed via the root mean squared error (RMSE), i.e., the standard deviation of the distribution of computed DOIs at each irradiated position. The achieved resolution is large compared to the width of the collimated beam, which is why no correction for the beam width will be applied. Each of the five parameters computed for each irradiated DOI position will be averaged to report their mean values over the whole length of the crystal.

4) TOF Resolution: At each irradiated DOI position and for all DOI positions combined, the CTR is evaluated by matching coincidences with a coincidence time window of 7.5 ns and selecting events $\pm 2\sigma$ around the photopeak in the raw energy value spectrum of the main channel and $\pm 2\sigma$ around the light-sharing peak in the adjacent channel. A Gaussian is fitted to the coincidence time difference histogram and the CTR is given as the FWHM, which corresponds to $2\sqrt{2\ln(2)}\sigma$. The obtained value CTR_{meas} is then corrected for the CTR of the reference CTR_{ref} using (2). The mean of the Gaussian shifts with the irradiated DOI position (c.f. Fig. 11(a) and (b)). To correct for the impact of the DOI on the measured CTR (CTR_{meas}), the ε-values of the head-on irradiation experiments are visualized in a scatter plot versus the measured coincidence time difference. A linear correction is applied to the timestamps based on the ε-value computed for each event according to (3)

$$t_{corr} = t_{meas} - v \cdot \varepsilon + w. \tag{6}$$

For the given setup, where the reference detector is not affected by a DOI-related photon time transfer spread, this results in a correction for the coincidence time differences Δt according to

$$\Delta t_{corr} = \Delta t_{meas} - v \cdot \varepsilon + w \tag{7}$$

where v and w are the slope and y-axis intercept of a linear fit applied to a scatter plot of the measured coincidence time difference versus the computed ε-value. Afterward, (2) is applied to the corrected time difference.

D. Coincidence Experiments With Head-On Unit Irradiation

Using the unit with the best-DOI encoding, we performed coincidence experiments with the detector unit to evaluate the CTR for different bias voltage and threshold settings with both HF readout electronics and the TOFPET2 ASIC. The TOF-DOI unit was aligned with the reference detector and source, keeping a larger distance between the unit and source to enable the irradiation of both unit channels (c.f. Figs. 5 and 7(b) for irradiation concept). The CTR is determined individually for each unit channel by matching coincidences with a coincidence time window of 7.5 ns and selecting events $\pm 2\sigma$ around the photopeak in the raw energy value spectrum of the main channel. A Gaussian is fitted to the remaining coincidence time difference histogram and the CTR is given as the FWHM and corrected for the CTR of the reference again using (2). Additionally, a CTR value corrected for the impact of the DOI is provided using (7).

IV. RESULTS

A. Reference Performance

The CTR of both crystals of each TOF-DOI unit is measured with HF readout electronics to investigate the TOF resolution limits of the proposed DOI concepts. As a sanity check, the CTR of both channels of the adapted HF readout board was measured with two $2 \times 2 \times 3\,mm^3$ LYSO:Ce crystals (Epic-crystal) on Broadcom AFBR-S4N33C013 SiPMs, one of which was used as reference detector in further measurements. Both channels achieved the same CTR of about
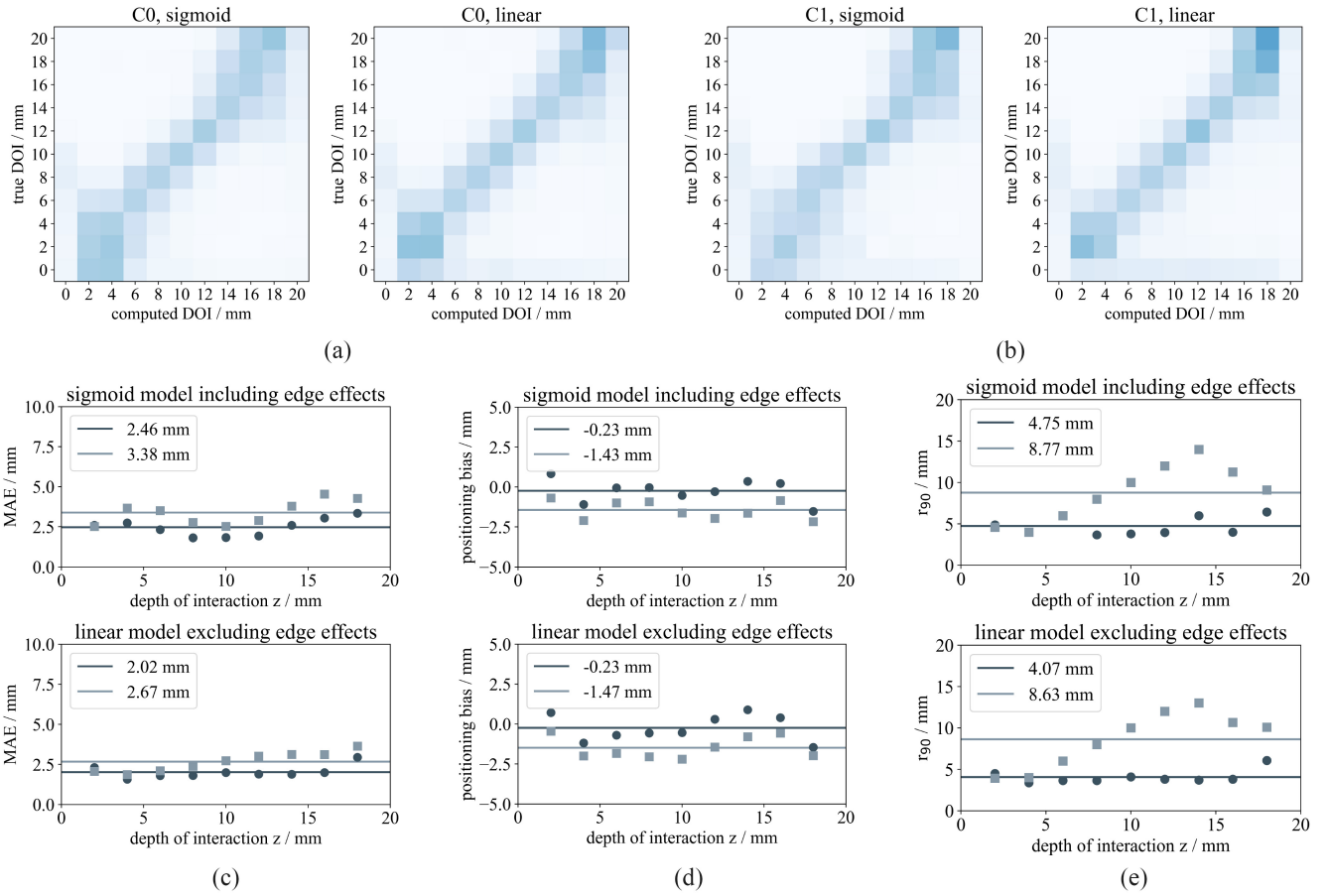
(a)

(b)

(c)

(d)

(e)

Fig. 10. Parameters to access the DOI-encoding performance of a given detector unit for the example of a triangular reflector sheet and TiO$_2$ coating (c.f. Fig. 3(c)) and events filtered to $\pm 2\sigma$ around the photopeak. (a) PSF applying a sigmoid DOI-encoding model. (b) PSF applying a linear DOI-encoding model. (c) MAE in positioning. (d) Positioning bias. (e) Percentile distance of positioning 90 % of the events correctly. Parameters are depicted for both crystals of the unit (C0 in darker color, C1 in lighter color). Horizontal lines display the mean values of the respective parameters.

(a)

(b)

(c)
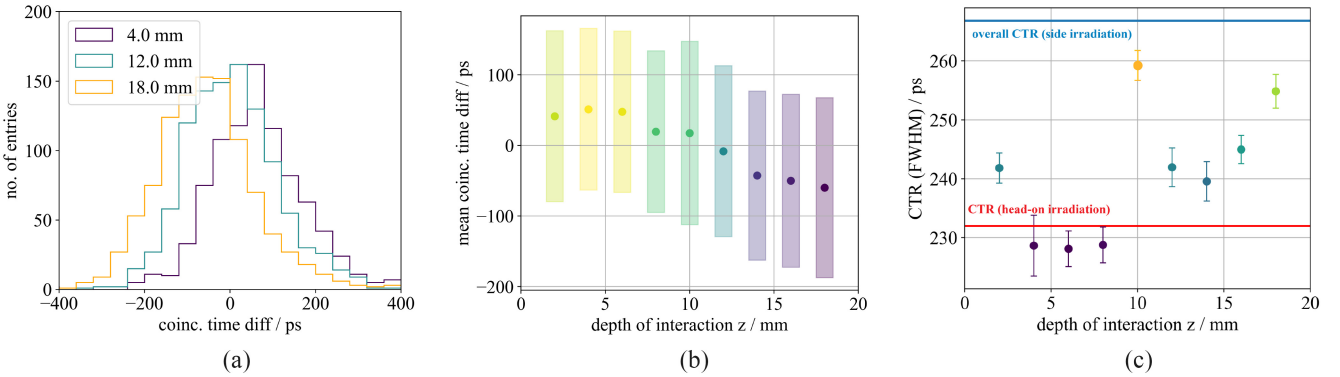
Fig. 11. Coincidence time difference and CTR depending on the DOI for the example of crystal C0 of a concept using a triangular reflector sheet and TiO$_2$ coating on a Broadcom AFBR-S4N33C013 SiPM (c.f. Fig. 3(c)). Depicted CTRs are not corrected for the CTR of the reference. (a) Coincidence time difference histograms shift slightly with the irradiated DOI. (b) Shift of the Gaussian centroid depending on the irradiated DOI. The boxes depict the CTR, i.e., the FWHM of the Gaussian. (c) Measured CTR depending on the DOI. The lines depict the measured CTR in a head-on irradiation experiment and for the coincidence time difference histograms evaluated on one combined histogram of all time differences measured at all irradiated DOIs (side irradiation).

70 ps (FWHM) within their statistical fluctuations, confirming that both channels of the adapted HF readout operate reliably and in the same way. For the TOFPET2 ASIC, a reference CTR of 134 ps (FWHM) was measured. In the following measurements with different TOF-DOI concepts, the CTR measured for the TOF-DOI unit against the reference was corrected for the reference CTR according to (2).

B. Beam Characterization

The FWHM of the Gaussian fit to the peaks indicating the crystal ends (c.f. Fig. 8) is an estimate for the actual width of the beam, which was determined to 1.4 mm.

C. DOI Capabilities With Collimated Radiation

Fig. 9 depicts the stages of the data processing to evaluate the DOI resolution of each TOF-DOI unit concept for the

TABLE I

ASSESSMENT OF THE DOI CAPABILITIES OF THE DIFFERENT UNIT CONCEPTS USING SIGMOID AND LINEAR MODULATION: THE DOI RESOLUTION IS REPORTED AS THE STANDARD DEVIATION OF THE DIFFERENCES BETWEEN TRUE AND COMPUTED DOIs. THE MAE IS THE MEAN OF THE ABSOLUTE VALUE OF THE DIFFERENCES BETWEEN TRUE AND COMPUTED DOIs. THE PERCENTILE DISTANCES r_{50} AND r_{90} REFER TO THE DISTANCE TO THE TRUE POSITION WITHIN WHICH 50 % AND 90 % OF THE EVENTS ARE POSITIONED. FOR ALL MODELS, EVENTS WHICH ARE POSITIONED AT DOIs $z > 20$ mm AND $z < 0$ mm WERE TRUNCATED AND POSITIONED AT $z = 20$ mm AND $z = 0$ mm, RESPECTIVELY. ALL VALUES REPORTED REFER TO THE AVERAGE OVER THE NINE VALUES REPORTED AT THE IRRADIATED POSITIONS ALONG THE LENGTH OF THE CRYSTAL

configuration / crystal	DOI res. (RMSE) / mm				MAE / mm				r_{50} / mm				r_{90} / mm			
	sigmoid		linear		sigmoid		linear		sigmoid		linear		sigmoid		linear	
	C0	C1	C0	C1	C0	C1	C0	C1	C0	C1	C0	C1	C0	C1	C0	C1
Broadcom AFBR-S4N33C013																
6 FP	5.3	9.4	5.9	8.8	6.0	8.7	4.9	8.1	5.6	6.0	4.3	5.6	9.2	14.4	10.1	14.4
DP half	6.9	6.3	9.7	7.8	8.4	7.9	9.4	7.4	8.7	5.5	7.6	5.9	14.4	13.1	14.4	14.4
DP triangle	6.9	6.5	6.1	5.6	6.1	5.0	6.1	5.4	5.0	4.5	5.5	4.6	11.4	12.1	13.0	12.1
DP triangle (2FDP)	7.0	6.4	6.9	6.4	6.2	5.4	6.0	5.4	5.4	4.3	5.5	4.6	12.7	12.2	13.3	12.6
2 carvings	5.8	6.5	4.9	5.9	5.2	5.7	4.4	5.1	5.3	5.3	3.9	4.5	8.0	11.5	8.3	11.2
5 carvings	5.1	5.2	4.3	4.8	4.3	4.4	3.6	4.0	3.4	3.4	3.0	3.1	7.2	10.5	7.1	10.4
ESR triangle + Meltmount, Teflon coating	5.2	5.4	4.1	4.7	4.4	4.4	3.5	3.7	3.5	3.2	2.8	2.7	7.5	10.4	7.1	10.4
ESR triangle + Meltmount, glued ESR coating	5.4	5.7	4.8	5.2	4.5	4.4	3.9	4.2	3.4	3.4	3.2	3.3	8.5	11.2	8.1	10.8
ESR triangle + Meltmount, TiO$_2$ coating	3.2	4.4	2.6	3.7	2.5	3.4	2.0	2.7	2.0	2.3	1.5	1.6	4.8	8.8	4.1	8.6
FBK NUV-MT ESR triangle + Meltmount, TiO$_2$ coating (@OV 9 V)	2.3	3.2	2.0	2.8	1.7	2.4	1.5	2.0	1.4	1.9	1.1	1.3	3.3	5.3	2.9	4.9

example of the configuration in Fig. 3(c) with TiO$_2$ coating read out with Broadcom AFBR-S4N33C013 SiPMs. The Gaussian centroids of the ε-histograms (c.f. Fig. 9(a)) are determined for each irradiated DOI and fit with a sigmoid or linear model (c.f. Fig. 9(b)). Afterward, the DOI of each event is computed and plotted as a histogram for each DOI label applying the model mentioned above (c.f. Fig. 9(c)).

Fig. 10 shows the computed PSF, MAE, bias and percentile distance r$_{90}$ for the example of the configuration in Fig. 3(c) with TiO$_2$ coating and read out with Broadcom AFBR-S4N33C013 SiPMs. Table I reports the mean values of these parameters for all investigated unit concepts in Fig. 3(a)–(f). With Broadcom AFBR-S4N33C013 SiPMs, the concepts achieved maximum DOI resolutions of on average between 2.6 and 8.8 mm (RMSE) considering both the sigmoid and linear model, with an improved resolution in the center of the crystal and a degradation toward the crystal ends. The MAE in positioning lies between 2.0 and 9.1 mm. Merely, the unit concept featuring two crystals, each with all six faces polished, shows a different behavior than all other unit concepts, with improved resolution toward both crystal ends but deteriorated resolution in the center of the crystal. The TOF-DOI unit concepts featuring carvings show distinctive local deterioration of the MAE related to the carvings at $z = 10$ mm. Triangular concepts exhibit an improved positioning accuracy toward the crystal edge coupled to the SiPM. The highest and most uniform positioning accuracy (MAE of 2.0 to 4.5 mm on average, c.f. Table I) was achieved for the TOF-DOI unit concept assembled according to Fig. 3(c) considering a linear

DOI-encoding model. Different coatings (Teflon, glued ESR and TiO$_2$) were tested for this configuration. Here, the unit with TiO$_2$ coating achieved the broadest uniformity (MAE of 2.0 to 2.7 mm, DOI resolution of 2.6 to 3.72 mm (RMSE), c.f. Table I) and was therefore as well coupled to two FBK NUV-MT SiPMs. This slightly improved the positioning accuracy and DOI resolution to on average 1.5 to 2.0 mm and 2.0 to 2.8 mm (RMSE) (c.f. Table I).

Concerning the PSF depicted in Fig. 10(a) and (b), a coarser binning was applied to display the accuracy of assigning the γ-events to one of four bins à 5 mm and one of two bins à 10 mm, respectively, as shown in Fig. 12. It is favored that this results in a diagonal matrix, implying high-positioning accuracy in all four bins or two bins. However, looking at the confusion matrices of the different TOF-DOI concepts investigated (examples shown Fig. 12) reveals that only the TOF-DOI concepts according to Fig. 3(c), (g) and (h) with Teflon coating show a diagonal confusion matrix (c.f. Fig. 12(b) and (c)) with approx. 70% to 95% of correctly positioned events in both of the two 10 mm bins. Moreover, the unit concept Fig. 3(c) with TiO$_2$ coating additionally achieves a position accuracy of approx. 48% to 75% in each of the four 5 mm bins (c.f. Fig. 12(c)). While other continuous DOI concepts struggle to accurately position events into four or two bins, completely polished crystals and carved DOI concepts seem to separate two layers quite well (c.f. Fig. 12(a) and (b)), reaching an accuracy higher than 64 % to 92 %. Not selecting events with an energy of $\pm 2\sigma$ around the photopeak and considering the unit concept Fig. 3(c) with TiO$_2$ coating again, the
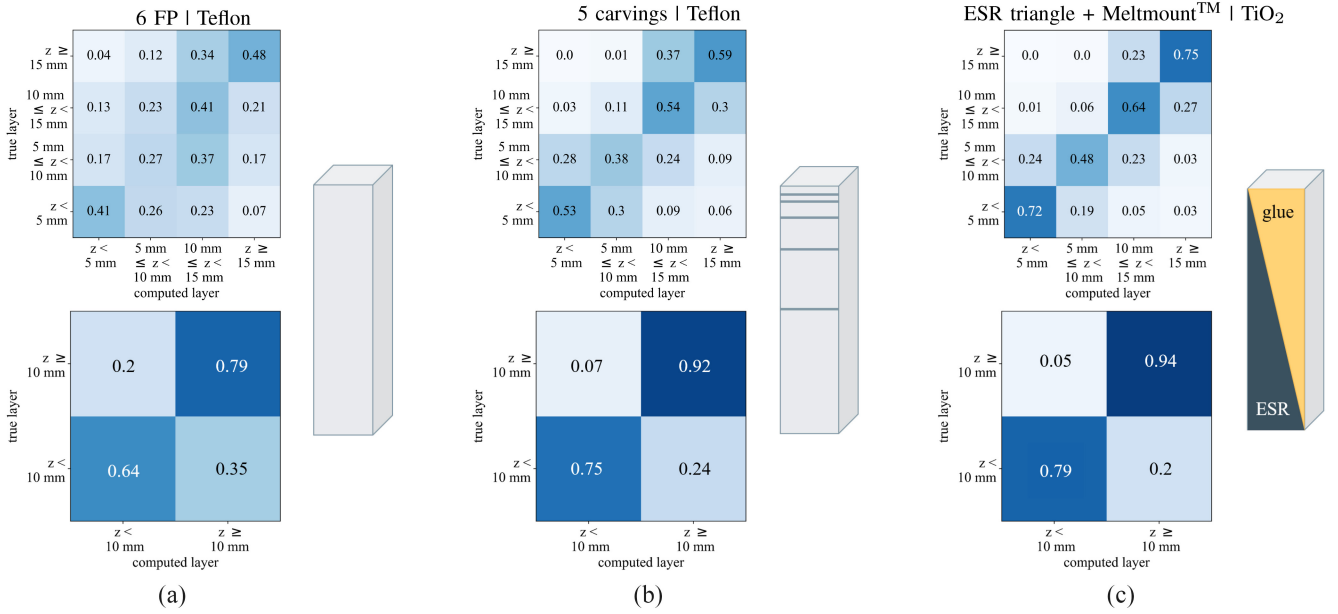
Fig. 12.   Positioning accuracy of the proposed DOI concepts for one crystal of the DOI unit (C0) assessed via the confusion matrix computed for a discrete DOI-layers of 5 mm or 10 mm width each, respectively. Events were selected based on their energy $\pm 2\sigma$ around the photopeak. The DOI has been computed via the sigmoid model. Results are shown for a TOF-DOI unit read out with Broadcom AFBR-S4N33C013 SiPMs. (a) 6 FP | Teflon wrapping. (b) 5 carvings | Teflon wrapping. (c) Triangular ESR cut out and Meltmount^{TM} | TiO$_2$ coating.

TABLE II
COMPARISON OF THE CTR OF THE DIFFERENT TOF-DOI CONCEPTS ACHIEVED IN *Side Irradiation* EXPERIMENTS WITH THE TOFPET2
ASIC WITH AND WITHOUT A DOI CORRECTION APPLIED AT AN OVERVOLTAGE OF 7.5 V. THE DOI CORRECTION WAS COMPUTED
BASED ON THE ε-VALUE. THE GIVEN CTRs HAVE BEEN CORRECTED FOR THE REFERENCE CTR. THE ERRORS REPORTED
CORRESPOND TO STATISTICAL ERRORS COMPUTED ACCORDING TO THE χ^2 DISTRIBUTION. EVENTS WERE SELECTED $\pm 2\sigma$
AROUND THE PHOTOPEAK AND THE RESPECTIVE LIGHT-SHARING PEAK IN THE ADJACENT CHANNEL

Configuration	$CTR_{TOFPET2,C0}$ (FWHM) / ps		$CTR_{TOFPET2,C1}$ (FWHM) / ps	
	w/o DOI corr.	with DOI corr.	w/o DOI corr.	with DOI corr.
Broadcom AFBR-S4N33C013 (3×3 mm^2)				
6 FP	253 ± 2	249 ± 2	255 ± 2	251 ± 2
DP half	315 ± 2	307 ± 2	333 ± 2	307 ± 2
DP triangle	274 ± 2	262 ± 2	334 ± 2	295 ± 2
DP triangle (2FDP)	345 ± 2	312 ± 2	358 ± 3	330 ± 2
2 carvings	320 ± 2	286 ± 2	355 ± 3	299 ± 2
5 carvings	277 ± 2	240 ± 2	287 ± 2	244 ± 2
ESR triangle + Meltmount, Teflon coating	279 ± 2	269 ± 2	293 ± 2	264 ± 2
ESR triangle + Meltmount, glued ESR coating	288 ± 2	273 ± 2	322 ± 2	296 ± 2
ESR triangle + Meltmount, TiO$_2$ coating	350 ± 3	314 ± 2	372 ± 3	323 ± 3
FBK NUV-MT (3×3 mm^2)				
ESR triangle + Meltmount, TiO$_2$ coating (@OV 9 V)	278 ± 3	226 ± 2	290 ± 3	233 ± 3

positioning accuracy deteriorates to 50 % in each of the four layers.

D. Impact of the DOI on the TOF Resolution in Experiments With Collimated Radiation

To quantify the impact of the DOI on the CTR, the TOF resolution of each unit channel is evaluated in combination with the TOFPET2 ASIC at each irradiated DOI. In both crystals of the unit, the centroid of the coincidence time difference histogram shifts with the irradiated DOI (c.f. Fig. 11(a) and (b)).

Additionally, the CTR achieved is highest at the crystal face furthest away from the SiPM, i.e., a DOI of $z = 0$ mm, and worsens toward the crystal face coupled to the SiPM, i.e., a DOI of $z = 20$ mm (c.f. Fig. 11(c)). Hence, the overall CTR, evaluated for the coincidence time difference histogram combining all data from the several measurements at different DOI, is worse than the individually determined CTRs. To correct the impact of the DOI on the CTR, a linear correction is applied according to (6) based on the ε-value computed for each event. Table II lists the measured CTR of all DOIs combined and the corrected CTR. The measured CTR ranges from 253 to
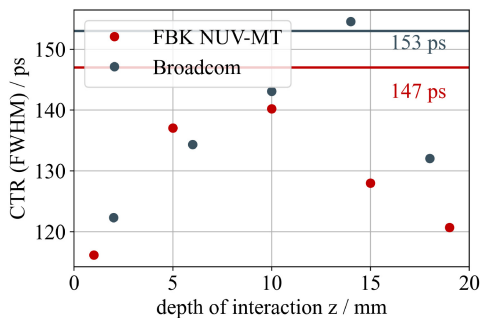
Fig. 13.   CTR dependent on the DOI for crystal C0 of the TOF-DOI unit concept employing a triangular ESR reflector sheet and TiO$_2$ coating (c.f. Fig. 3(c)) read out by Broadcom AFBR-S4N33C013 SiPMs and FBK NUV-MT SiPMs and HF electronics. The depicted CTR is corrected for the reference CTR but not for DOI effects. Horizontal lines indicate the values measured in head-on experiments.

372 ps and can be improved to 226 to 323 ps with the linear correction (c.f. Table II). It is striking that the CTR of the DOI concepts achieving a higher-DOI resolution benefits more from the applied DOI correction method. The benefit from the correction is generally more prominent than in head-on irradiation experiments. Additionally, it has to be noted that crystal C1 always performs worse than crystal C0, which probably is an effect of the setup to be discussed below.

For comparison, measurements with collimated radiation have been conducted for the unit concept using a triangular ESR reflector sheet and TiO$_2$ coating using HF electronics. These scans show a parabolic dependency of the CTR on the irradiated DOI for both Broadcom AFBR-S4N33C013 and FBK NUV-MT SiPMs, resulting in an improved CTR toward the crystal top and bottom (c.f. Fig. 13).

E. TOF Resolution in Head-On Coincidence Experiments

The TOF-DOI unit with the most promising DOI resolution (c.f. Section IV-C) was mounted and measured on FBK NUV-MT SiPMs, which achieved a CTR of 147 ps (FWHM) using HF electronics and boosted the CTR to 235 ps (FWHM) using TOFPET2 electronics (c.f. Fig. 14). Using a linear DOI correction, this can be further improved to 141 ps (FWHM) and 226 ps (FWHM), respectively. The performance is again degraded compared to a single pixel (Broadcom NUV-MT SiPMs, 3.8×3.8 mm^2) achieving 95 ps (FWHM) compared to 157 ps (FWHM), respectively [29]. This comparison has to be treated with caution, as two different SiPM types (FBK NUV-MT, Broadcom NUV-MT) with different active areas were applied, but it is the closest to be found in the literature.

F. Combining TOF and DOI Resolution

To select suitable configurations for assembling TOF-DOI matrices, Fig. 15 maps the achievable TOF resolution against the achievable DOI resolution computed for all TOF-DOI unit concepts. If the TOF-DOI unit was read out with the TOFPET2 ASIC, the graph shows no direct correlation between the CTR and the DOI resolution but an overall deterioration of 20 % to 45 %. However, switching to a different sensor technology (FBK NUV-MT) boosts the CTR, as reported before [29]. For HF readout electronics, the CTR of the investigated concepts
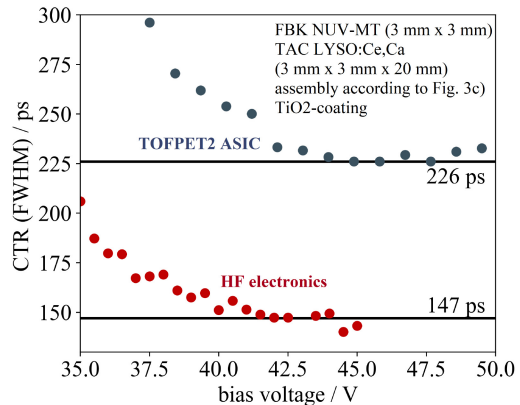

Fig. 14.   CTR dependent on the applied bias voltage for a TOF-DOI unit consisting out of two FBK NUV-MT SiPMs (3×3 mm^2) and two LYSO:Ce,Ca crystals (TAC; $3 \times 3 \times 20$ mm^3) assembled according to Fig. 3(c) with TiO$_2$ coating.
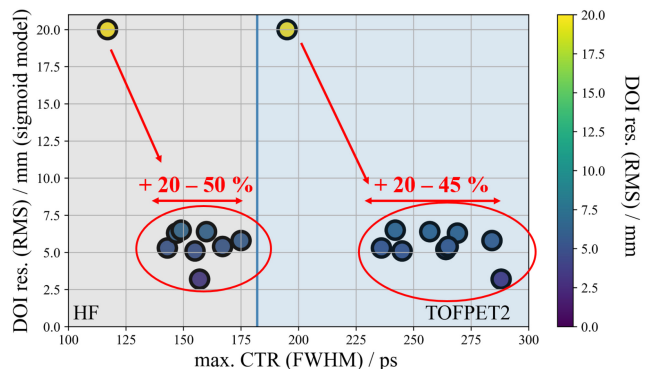

Fig. 15.   Correlation between maximum CTR (FWHM) and DOI capabilities of the unit: DOI resolution (RMSE) versus achievable CTR for the different unit concepts read out by Broadcom AFBR-S4N33C013 SiPMs.

lies in the same range and shows a deterioration of 20 % to 50 % compared to a single channel. This includes the measurement with FBK NUV-MT SiPMs. We identify the TOF-DOI unit concept using a triangular reflector sheet in combination with an optical coupling medium (c.f. Fig. 3(c)) and TiO$_2$ coating coupled to FBK NUV-MT SiPMs as the currently best option to realize high-TOF and high-DOI resolution at the same time.

V. DISCUSSION

A. Event Processing

The coincident raw energy value spectra of each crystal in a unit, as depicted in Fig. 6, show distinctive features, such as the photopeak attributed to a γ-interaction, depositing roughly 511 keV in one crystal with a corresponding peak at lower raw energy values in the adjacent channel. Additionally, the Compton continuum attributed to Compton scattered events and a backscatter peak (scatter angle of 180° resulting in an energy deposition of (2/3) of the photopeak energy). This becomes visible when irradiating the unit with collimated radiation from the side. It can be distinguished well from the light-sharing peak, located at approximately (1/3) of the photopeak energy according to the computed energy ratios. The backscatter peak is only visible in one of the crystals'

raw energy value spectra, i.e., the crystal located between the source and the second crystal of the unit, as this is the only crystal that can register backscattered events from the other crystal. If a backscatter occurs in this crystal itself (C1; the crystal closer to the source), the scattered γ-photon leaves the unit and no additional peak is visible in the raw energy value spectrum of the adjacent channel. Using energy filters $\pm 2\sigma$ of the photopeak and respective light-sharing peak in both energy channels for each crystal should prevent scatter from influencing the modeling of the DOI encoding. This results in a fraction of 44 % to 48 % of remaining detected coincidences. In side irradiation experiments, crystal C1 is the crystal always performing worse than the adjacent one (C0), which hints that carefully selecting events within $\pm 2\sigma$ of the photopeak and light-sharing peak might not be entirely sufficient to prevent the influence of scatter.

B. Beam Characterization

As all DOI resolutions (reported as RMSE) are comparably large with respect to the width of the collimated beam (reported as FWHM), we do not expect the beam width to contribute to the measured DOI resolution, which is why no correction for the beam width is applied.

C. DOI Capabilities With Collimated Radiation

The investigated TOF-DOI unit concepts achieve average DOI resolutions in the order of other state-of-the-art concepts. Most concepts show improved positioning accuracy in the center of the crystal with a deterioration toward the crystal ends.

The TOF-DOI unit consisting of two crystals with all six faces polished was expected not to resolve any DOI information. The improvement of the DOI resolution toward the crystal ends seen for this concept is probably an effect of the crystal surfaces. Concepts involving glue coupling between the two crystals show an improved DOI resolution compared to the other units. This is most likely due to a change of the limit angle of total internal reflection of the crystal-Meltmount gap compared to a crystal-air gap and, thus, facilitated light-sharing between the two channels.

Depolished, i.e., roughened parts of crystal surfaces change the specular reflection to diffusive reflection, hindering the refraction of light into the neighboring crystal. This is why the depolished half and triangular surfaces have been oriented toward the SiPM. Generally, a roughened surface could also result in a position-encoded light output on the SiPM due to the loss of optical photons, which are reflected to the top of the crystal and not guided toward the sensor. Therefore, these concepts might provide a similar DOI resolution when turned upside down. However, this would probably also change the behavior of the ε-values.

In line with this, the glue-coupled unit with TiO_2 coating achieved the best-DOI resolution, most likely as TiO_2 acts as a diffusive medium and additionally absorbs some of the optical photons, resulting in a position-encoded light output of the pixel. Using the same unit concept, FBK NUV-MT SiPMs can further boost the DOI resolution, most likely due to

reduced internal crosstalk and an improved energy resolution, positively influencing the DOI encoding via the variable ε. Distinguishing at least two and up to four DOI bins, this concept can be used to pass the DOI information to image reconstruction algorithms to reduce parallax errors. While a linear model is likely to provide a more uniform DOI resolution over the crystal length, which would be essential for accurately recovering Compton scattered events, and can be fit to the margins of the ε-distribution to enable in-system calibration (see below), the sigmoid function may provide more accurate modeling for the S-shaped ε-curves. Therefore, it locally results in an improved resolution with a larger deterioration at the crystal ends. Resolving coarse DOI bins uniformly over the whole length of the crystal for image reconstruction, e.g., two or four regions, hence might benefit from using a linear model over a sigmoid model, which would also become relevant considering in-system calibration (see also Section V-F). The general improvement to be expected by passing DOI information to the reconstruction algorithm in terms of the SNR and quality of the resulting PET images has to be quantified in simulations.

D. Impact of the DOI on the TOF Resolution in Experiments With Collimated Radiation

Not applying any corrections or collimation, the overall CTR in side-irradiation experiments is expected to deteriorate compared to head-on irradiation, as for the experiments conducted, all irradiated DOIs contribute equally to the measured CTR. The overall coincidence time difference histogram broadens due to the shift of the Gaussian centroid caused by runtime differences due to different DOI. Additionally, the individual histograms are broader, i.e., the CTR is worse for DOI close to the SiPM. This can be explained by two optical photon waves, one consisting of direct optical photons and the other one of reflected optical photons, which arrive at the SiPM at different points in time as simulated by Gundacker et al. [10] and Loignon-Houle et al. [58]. They cause a smearing of the rising edge of the signal pulse, which in turn causes a worse CTR. For the case of DOIs furthest away from the SiPM, the optical photon waves reach the SiPM with a more negligible time difference, resulting in a steep rising edge of the signal and no deterioration of the CTR. This is why the CTR in head-on irradiation experiments is better than the average CTR for all DOIs, as for head-on irradiation, the more shallow DOIs at the top of the crystal contribute to a larger weight. Applying a linear correction for the DOI impact on the CTR, i.e., correcting the shifts of the Gaussian centroid with the DOI, results in a significant improvement of the achieved CTR, which is close to head-on coincidence experiments (c.f. Table II). Regarding the parabolic dependency of the CTR over the DOI in experiments with HF readout electronics, a similar effect has been observed for LYSO:Ce,Ca and BaF_2:Y crystals in Herweg et al. [59], which has been attributed to the capability of the readout electronics to resolve two waves of incident optical photons on the SiPM, i.e., the direct and the optical photons reflected at the top, as also described by Loignon-Houle et al. [58] and Gundacker et al. [10].

For all TOF-DOI unit concepts investigated in experiments with collimated source activity and the TOFPET2 ASIC, crystal C1 performs worse than crystal C0. Since each TOF-DOI unit was aligned in line with the collimated beam (c.f. Fig. 7(a)), there is one channel stopping more γ-photons than the other according to the law of Lambert–Beer. As the channel first in line is channel B, the deterioration of the CTR observed for this channel could be a statistical effect, as the applied energy filter should reliably exclude backscattered events.

E. TOF Resolution in Head-on Coincidence Experiments

In head-on irradiation coincidence experiments, the CTR of all investigated TOF-DOI unit concepts was worse than measured for single pixels (c.f. Fig. 15), which is presumably due to the impact of light-sharing and crosstalk between the two channels. The degradation of the CTR of the TOF-DOI unit using FBK NUV-MT SiPMs with the HF electronics might be caused by a common cathode, which deteriorates the signal read from the cathode in the case of the HF electronics. Furthermore, it is possible that the TiO$_2$ coating of the detector unit deteriorates the timing by its reflective behavior. The linear DOI correction applied to the coincidence time difference leads to a smaller improvement for head-on than for side-irradiation experiments, which is probably due to less deep DOIs being irradiated according to the law of Lambert–Beer. Another reason could be a less accurate linear approximation of the DOI dependency on the ε-values computed from head-on irradiation data, which was done to investigate the possibility of in-system calibration of the DOI encoding without the requirement of previous, external calibration measurements. The fact that the achievable CTR seems to be influenced by the chosen light-sharing method for the TOFPET2 readout shows that the ASIC's electronic front end and trigger circuit do not respond well to a smeared rising edge due to light-sharing. In the same way, the HF electronics show a deterioration of the CTR, despite this front end being capable of triggering on the first direct photons arriving, extracting the timing information based on these. The deterioration of the CTR in both cases is about 30 % compared to a single-pixel measurement (c.f. Fig. 15), which fits the range of computed ε-values, i.e., indicates a link to the light-sharing ratio.

F. Combining TOF and DOI Resolution (In-System Calibration of the DOI-Encoding Variable)

Fig. 16 shows the distribution of ε measured in the scans with collimated radiation from the side, flood irradiation from the side and head-on irradiation for the example of a unit concept using a triangular reflector sheet and TiO$_2$ coating (c.f. Fig. 3(c)) read out by Broadcom AFBR-S4N33C013 SiPMs. While collimated irradiation from the side results in clear margins, which are matched by flood irradiation from the side and allow to deduce the DOI encoding via a linear fit, the distribution of the ε-value in head-on irradiation experiments is slightly distorted and shifted. The heights of the visible peaks and the distortion also indicate an asymmetric irradiation of the TOF-DOI unit, where the right histogram side was aligned and the left was not, which would match the observation of a worse
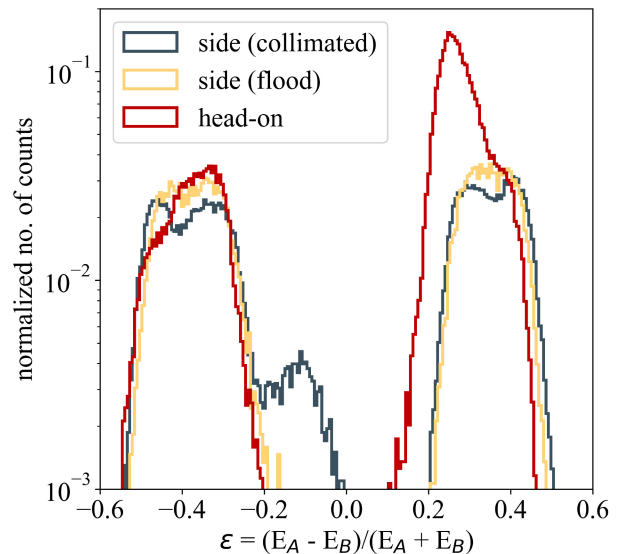

Fig. 16. Distribution of the DOI-encoding variable ε for the example of the unit concept using a triangular reflector sheet and TiO$_2$ coating [c.f. Fig. 3(c)] read out by Broadcom AFBR-S4N33C013 SiPMs at an applied overvoltage of 7.5 V. The histogram shows the ε-distribution for both crystals for head-on, side, and collimated side irradiation.

CTR for one of the channels due to alignment issues. A correction of the obtained ε-distribution according to the law of Lambert–Beer could solve the distortion effect. Considering a PET system, it is likely that a range of deeper DOIs is shielded by neighboring detectors, which might result in the same distortion and potentially limit the DOI correction applied - unless a correction according to the law of Lambert–Beer is applied. Using the lutetium background might help to overcome this issue [60]. It has to be evaluated whether simulation techniques [61], as developed for monolithic scintillators, could be applied here as well. As Fig. 16 shows, applying a linear model to assign the DOI using the margins of the ε-distribution without an external calibration would still be possible. Hence, the applied DOI concept might offer an in-system calibration without the need for collimation or individual calibration of single detector elements.

VI. CONCLUSION

Regarding the performance limits of the units, the trade-off between timing and DOI-encoding becomes apparent for TOFPET2 readout. In contrast, the performance with HF readout electronics suffers only slightly from a deteriorated CTR due to light-sharing effects. The best-performing unit concept was achieved with a combination of triangular reflector sheets, optical coupling medium and TiO$_2$-coating read out by FBK NUV-MT SiPMs. Using the TOFPET2 ASIC for readout, it has an average DOI resolution of approx. 2 to 3 mm (RMSE), while achieving a state-of-the-art CTR of 226 ps (FWHM) when applying a linear DOI correction. The same unit achieved a CTR of 141 ps (FWHM) using HF readout and the same correction method. Apart from simplicity and scalability, this detector design does not necessarily require an external calibration of the DOI-encoding variable ε, as a linear fit and DOI encoding could already be realized using the

margins of the ε-distribution. This makes the proposed concept very interesting for system integration and favors a linear DOI-encoding model over more complex models.

ACKNOWLEDGMENT

REFERENCES

[1] Alzheimer's Association, "2021 Alzheimer's disease facts and figures," *Alzheimer's Dementia*, vol. 17, no. 3, pp. 327–406, 2021. [Online]. Available: https://alz-journals.onlinelibrary.wiley.com/doi/abs/10.1002/alz.12328

[2] W. Bao, F. Xie, C. Zuo, Y. Guan, and Y. H. Huang, "PET neuroimaging of Alzheimer's disease: Radiotracers and their utility in clinical research," *Front. Aging Neurosci.*, vol. 13, May 2021, Art. no. 624330. [Online]. Available: https://www.frontiersin.org/articles/10.3389/fnagi.2021.624330

[3] S. R. Cherry and M. Dahlbom, *PET: Physics, Instrumentation, and Scanners*. New York, NY, USA: Springer, 2006, pp. 1–117. [Online]. Available: https://doi.org/10.1007/0-387-34946-4_1

[4] S. Vandenberghe, E. Mikhaylova, E. D'Hoe, P. Mollet, and J. S. Karp, "Recent developments in time-of-flight PET," *EJNMMI Phys.*, vol. 3, no. 1, p. 3, 2016. [Online]. Available: https://www.ncbi.nlm.nih.gov/pubmed/26879863

[5] S. Surti, "Update on time-of-flight PET imaging," *J. Nucl. Med.*, vol. 56, no. 1, pp. 98–105, 2015. [Online]. Available: https://jnm.snmjournals.org/content/56/1/98

[6] M. Conti, "Focus on time-of-flight PET: The benefits of improved time resolution," *Eur. J. Nucl. Med. Mol. Imag.*, vol. 38, pp. 1147–1157, Jan. 2011. [Online]. Available: https://link.springer.com/article/10.1007/s00259-010-1711-y

[7] S. Surti and J. S. Karp, "Update on latest advances in time-of-flight PET," *Physica Medica*, vol. 80, pp. 251–258, Dec. 2020. [Online]. Available: https://www.sciencedirect.com/science/article/pii/S112017972030274X

[8] T. Tomitani, "Image reconstruction and noise evaluation in photon time-of-flight assisted positron emission tomography," *IEEE Trans. Nucl. Sci.*, vol. 28, no. 6, pp. 4581–4589, Dec. 1981.

[9] M. Conti, "State of the art and challenges of time-of-flight PET," *Physica Medica*, vol. 25, no. 1, pp. 1–11, 2009. [Online]. Available: https://www.sciencedirect.com/science/article/pii/S1120179708000975

[10] S. Gundacker, A. Knapitsch, E. Auffray, P. Jarron, T. Meyer, and P. Lecoq, "Time resolution deterioration with increasing crystal length in a TOF-PET system," *Nucl. Instrum. Methods Phys. Res. A, Accelerators, Spectrometers, Detectors Assoc. Equip.*, vol. 737, pp. 92–100, Feb. 2014. [Online]. Available: https://www.sciencedirect.com/science/article/pii/S0168900213015647

[11] C. L. Melcher, "Scintillation crystals for PET," *J. Nucl. Med.*, vol. 41, no. 6, pp. 1051–1055, 2000. [Online]. Available: https://pubmed.ncbi.nlm.nih.gov/10855634/

[12] M. Korzhik et al., "Development of scintillation materials for PET scanners," *Nucl. Instrum. Methods Phys. Res. A, Accelerators, Spectrometers, Detectors Assoc. Equip.*, vol. 571, no. 1, pp. 122–125, 2007.

[13] A. J. González, F. Sánchez, and J. M. Benlloch, "Organ-dedicated molecular imaging systems," *IEEE Trans. Radiat. Plasma Med. Sci.*, vol. 2, no. 5, pp. 388–403, Sep. 2018.

[14] X. Zeng et al., "A conformal TOF–DOI prism-PET prototype scanner for high-resolution quantitative neuroimaging," *Med. Phys.*, vol. 50, no. 6, pp. 3401–3417, Feb. 2023. [Online]. Available: https://doi.org/10.1002/mp.16223

[15] "Siemens healthineers—Biograph vision quadra." 2022. Accessed: Nov. 19, 2022. [Online]. Available: https://www.siemens-healthineers.com/de/molecular-imaging/pet-ct/biograph-vision-quadra

[16] S. Vandenberghe, P. Moskal, and J. S. Karp, "State of the art in total body PET," *EJNMMI Phys.*, vol. 7, p. 35, Dec. 2020. [Online]. Available: https://www.ncbi.nlm.nih.gov/pmc/articles/PMC7248164/

[17] S. Vandenberghe, "Progress and perspectives in total body PET systems instrumentation," *Bio-Algorithms Med-Syst.*, vol. 17, no. 4, pp. 265–267, 2021. [Online]. Available: https://doi.org/10.1515/bams-2021-0187

[18] S. R. Cherry, T. Jones, J. S. Karp, J. Qi, W. W. Moses, and R. D. Badawi, "Total-body PET: Maximizing sensitivity to create new opportunities for clinical research and patient care," *J. Nucl. Med.*, vol. 59, no. 1, pp. 3–12, 2018. [Online]. Available: https://jnm.snmjournals.org/content/59/1/3

[19] V. Nadig, K. Herrmann, F. M. Mottaghy, and V. Schulz, "Hybrid total-body pet scanners—Current status and future perspectives," *Eur. J. Nucl. Med. Mol. Imag.*, vol. 49, pp. 445–459, Jan. 2022. [Online]. Available: https://link.springer.com/article/10.1007/s00259-021-05536-4

[20] I. Mohammadi, I. F. C. Castro, P. M. M. Correia, A. L. M. Silva, and J. F. C. A. Veloso, "Minimization of parallax error in positron emission tomography using depth of interaction capable detectors: Methods and apparatus," *Biomed. Phys. Eng. Exp.*, vol. 5, no. 6, Oct. 2019, Art. no. 62001. [Online]. Available: https://dx.doi.org/10.1088/2057-1976/ab4a1b

[21] "Siemens healthineers—Biograph vision." 2022. Accessed: Nov. 19, 2022. [Online]. Available: https://www.siemens-healthineers.com/nl/molecular-imaging/pet-ct/biograph-vision

[22] D. Schug et al., "PET performance and MRI compatibility evaluation of a digital, ToF-capable PET/MRI insert equipped with clinical scintillators," *Phys. Med. Biol.*, vol. 60, no. 18, pp. 7045–7067, Aug. 2015. [Online]. Available: https://doi.org/10.1088/0031-9155/60/18/7045

[23] S. Vinogradov, "Approximations of coincidence time resolution models of scintillator detectors with leading edge discriminator," *Nucl. Instrum. Methods Phys. Res. Sect. A, Accelerators, Spectrometers, Detect. Assoc. Equip.*, vol. 912, pp. 149–153, Dec. 2018.

[24] F. Acerbi and S. Gundacker, "Understanding and simulating SiPMs," *Nucl. Instrum. Methods Phys. Res. Sect. A, Accelerators, Spectrometers, Detect. Assoc. Equip.*, vol. 926, pp. 16–35, May 2019. [Online]. Available: https://www.sciencedirect.com/science/article/pii/S0168900218317704

[25] M. Krake, V. Nadig, V. Schulz, and S. Gundacker, "Power-efficient high-frequency readout concepts of SiPMs for TOF-PET and HEP," *Nucl. Instrum. Methods Phys. Res. Sect. A, Accelerators, Spectrometers, Detect. Assoc. Equip.*, vol. 1039, Art. no. 167032, Sep. 2022, doi: 10.1016/j.nima.2022.167032.

[26] S. Gundacker, R. M. Turtos, E. Auffray, M. Paganoni, and P. Lecoq, "High-frequency SiPM readout advances measured coincidence time resolution limits in TOF-PET," *Phys. Med. Biol.*, vol. 64, no. 5, Feb. 2019, Art. no. 55012. [Online]. Available: https://doi.org/10.1088/1361-6560/aafd52

[27] S. Gundacker et al., "Experimental time resolution limits of modern SiPMs and TOF-PET detectors exploring different scintillators and Cherenkov emission," *Phys. Med. Biol.*, vol. 65, no. 2, Jan. 2020, Art. no. 25001. [Online]. Available: https://iopscience.iop.org/article/10.1088/1361-6560/ab63b4

[28] J. W. Cates, S. Gundacker, E. Auffray, P. Lecoq, and C. S. Levin, "Improved single photon time resolution for analog SiPMs with front end readout that reduces influence of electronic noise," *Phys. Med. Biol.*, vol. 63, no. 18, Sep. 2018, Art. no. 185022. [Online]. Available: https://doi.org/10.1088/1361-6560/aadbcd

[29] V. Nadig et al., "Timing advances of commercial divalent-ion co-doped LYSO:Ce and SiPMs in sub-100 ps time-of-flight positron emission tomography," *Phys. Med. Biol.*, vol. 68, no. 7, Feb. 2023, Art. no. 75002. [Online]. Available: https://iopscience.iop.org/article/10.1088/1361-6560/acbde4

[30] A. Gonzalez-Montoro, S. Pourashraf, M. S. Lee, J. W. Cates, and C. S. Levin, "Design considerations for PET detectors with 100 picoseconds coincidence time resolution," *Nucl. Instrum. Methods Phys. Res. Sect. A, Accelerators, Spectrometers, Detect. Assoc. Equip.*, vol. 1045, Jan. 2023, Art. no. 167579. [Online]. Available: https://www.sciencedirect.com/science/article/pii/S0168900222008713

[31] M. Ito, S. J. Hong, and J. S. Lee, "Positron emission tomography (PET) detectors with depth-of-interaction (DOI) capability," *Biomed. Eng. Lett.*, vol. 1, no. 2, pp. 70–81, 2011.

[32] Q. Xie, D. Xi, J. Zhu, and L. Wang, "Multilayer scintillation crystal and pet detector," U.S. Patent 9 395 452 B2, Jul. 2012.

[33] P. M. J. Dueppenbecker and T. Solf, "Modelling of ToF-DOI detector arrays," U.S. Patent 20 140 231 655 A1, May 2016.

[34] H. K. Wieczorek, T. Solf, and T. Frach, "Gamma radiation detector with parallax compensation," U.S. Patent 20 200 284 922, Sep. 2020.

[35] T. Lewellen, R. Miyaoka, and A. F. Zerrouk, "Scintillation detector for positron emission tomography," U.S. Patent 7 956 331 B2, Jun. 2011.

[36] S. McCallum, P. Clowes, and A. Welch, "A multilayer detector for PET based on APD arrays and continuous crystal elements," in *Proc. IEEE Symp. Conf. Rec. Nucl. Sci.*, vol. 5, 2004, pp. 2898–2902.

[37] V. Schulz et al., "Improving the diagnosis of breast cancer using a dedicated PET/MRI—The EU project HYPMED," *Nuklearmedizin*, vol. 59, no. 2, p. 147, 2020.

[38] S. Naunheim et al., "The HYPMED PET/MRI insert for enhanced diagnosis of breast cancer," in *Proc. PSMR-TBP*, 2022, p. 1. [Online]. Available: https://www.researchgate.net/publication/361951942_The_HYPMED_PETMRI_Insert_for_Enhanced_Diagnosis_of_Breast_Cancer

[39] C. S. Levin, "Promising new photon detection concepts for high-resolution clinical and preclinical PET," *J. Nucl. Med.*, vol. 53, no. 2, pp. 167–170, 2012. [Online]. Available: https://jnm.snmjournals.org/content/53/2/167

[40] T. Lewellen, M. Janes, and R. Miyaoka, "DMice—A depth-of-interaction detector design for PET scanners," in *Proc. IEEE Symp. Conf. Rec. Nucl. Sci.*, vol. 4, 2004, pp. 2388–2392.

[41] R. S. Miyaoka, T. K. Lewellen, H. Yu, and D. L. McDaniel, "Design of a depth of interaction (DOI) PET detector module," *IEEE Trans. Nucl. Sci.*, vol. 45, no. 3, pp. 1069–1073, Jun. 1998. [Online]. Available: https://ieeexplore.ieee.org/stamp/stamp.jsp?tp=&arnumber=681980&tag=1

[42] M. S. Lee and J. S. Lee, "Depth-of-interaction measurement in a single-layer crystal array with a single-ended readout using digital silicon photomultiplier," *Phys. Med. Biol.*, vol. 60, no. 16, pp. 6495–6514, Aug. 2015. [Online]. Available: https://doi.org/10.1088/0031-9155/60/16/6495

[43] M. Seo, H. Park, S. Lee, G. B. Ko, and J. S. Lee, "Depth-of-interaction positron emission tomography detector with 45° tilted silicon photo-multipliers using dual-ended signal readout," *Med. Phys.*, vol. 50, no. 7, pp. 4112–4121, Mar. 2023. [Online]. Available: https://doi.org/10.1002/mp.16355

[44] F. Mueller, D. Schug, P. Hallen, J. Grahe, and V. Schulz, "Gradient tree boosting-based positioning method for monolithic scintillator crystals in positron emission tomography," *IEEE Trans. Radiat. Plasma Med. Sci.*, vol. 2, no. 5, pp. 411–421, Sep. 2018. [Online]. Available: https://ieeexplore.ieee.org/abstract/document/8360486

[45] F. Mueller, D. Schug, P. Hallen, J. Grahe, and V. Schulz, "A novel DOI positioning algorithm for monolithic scintillator crystals in PET based on gradient tree boosting," *IEEE Trans. Radiat. Plasma Med. Sci.*, vol. 3, no. 4, pp. 465–474, Jul. 2019. [Online]. Available: https://ieeexplore.ieee.org/abstract/document/8554136

[46] F. Mueller, S. Naunheim, Y. Kuhl, D. Schug, T. Solf, and V. Schulz, "A semi-monolithic detector providing intrinsic DOI-encoding and sub-200 ps CRT TOF-capabilities for clinical PET applications," *Med. Phys.*, vol. 49, no. 12, pp. 7469–7488, 2022. [Online]. Available: https://aapm.onlinelibrary.wiley.com/doi/abs/10.1002/mp.16015

[47] K. Krueger, F. Mueller, P. Gebhardt, B. Weissler, D. Schug, and V. Schulz, "High-throughput FPGA-based inference of gradient tree boosting models for position estimation in PET detectors," *IEEE Trans. Radiat. Plasma Med. Sci.s*, vol. 7, no. 3, pp. 253–262, Mar. 2023. [Online]. Available: https://ieeexplore.ieee.org/document/10024309

[48] S. Naunheim, Y. Kuhl, T. Solf, D. Schug, V. Schulz, and F. Mueller, "Analysis of a convex time skew calibration for light sharing-based PET detectors," *Phys. Med. Biol.*, vol. 68, no. 2, Jan. 2023, Art. no. 25013. [Online]. Available: https://doi.org/10.1088/1361-6560/aca872

[49] L. Zheng, K. Shimazoe, Y. Yoshihara, A. Koyama, and H. Takahashi, "Development of a dual-sided readout DOI-PET detector using 500-μm-pitch 64-ch SiPMs," *J. Instrum.*, vol. 14, no. 4, Apr. 2019, Art. no. C04001. [Online]. Available: https://dx.doi.org/10.1088/1748-0221/14/04/C04001

[50] J. Huber, W. Moses, M. Andreaco, and O. Petterson, "A LSO scintillator array for a PET detector module with depth of interaction measurement," in *Proc. IEEE Nucl. Sci. Symp. Conf. Rec.*, vol. 2, 2000, pp. 46–50.

[51] C. Casella, M. Heller, C. Joram, and T. Schneider, "A high resolution TOF-PET concept with axial geometry and digital SiPM readout," *Nucl. Instrum. Methods Phys. Res. Sect. A, Accelerators, Spectrometers, Detect. Assoc. Equip.*, vol. 736, pp. 161–168, Feb. 2014. [Online]. Available: https://www.sciencedirect.com/science/article/pii/S0168900213014307

[52] S. Niedzwiecki et al., "J-PET: A new technology for the whole-body pet imaging," *Acta Physica Polonica B*, vol. 48, no. 10, pp. 1567–1575, 2017. [Online]. Available: https://www.actaphys.uj.edu.pl/fulltext?series=Reg&vol=48&page=1567

[53] A. Gola, C. Piemonte, and A. Tarolli, "Analog circuit for timing measurements with large area SiPMs coupled to LYSO crystals," in *Proc. IEEE Nucl. Sci. Symp. Conf. Rec.*, 2011, pp. 725–731.

[54] "AFBR-S4N66P024M product Webpage." Broadcom. Accessed: Feb. 8, 2023. [Online]. Available: https://www.broadcom.com/products/optical-sensors/silicon-photomultiplier-sipm/afbr-sApr.nJun.Jun.pFeb.Apr.m

[55] R. Bugalho et al., "Experimental characterization of the TOFPET2 ASIC," *J. Instrum.*, vol. 14, no. 3, Mar. 2019, Art. no. P03029.

[56] K. Weindel, V. Nadig, K. Herweg, V. Schulz, and S. Gundacker, "A time-based double-sided readout concept of 100 mm LYSO:Ce,Ca fibres for future axial TOF-PET," *EJNMMI Phys.*, vol. 10, no. 1, p. 43, Feb. 2023. [Online]. Available: https://link.springer.com/article/10.1186/s40658-023-00563-6

[57] C. Ritzer, P. Hallen, D. Schug, and V. Schulz, "Intercrystal scatter rejection for pixelated PET detectors," *IEEE Trans. Radiat. Plasma Med. Sci.*, vol. 1, no. 2, pp. 191–200, Mar. 2017. [Online]. Available: https://doi.org/10.1109/tns.2017.2664921

[58] F. Loignon-Houle et al., "DOI estimation through signal arrival time distribution: A theoretical description including proof of concept measurements," *Phys. Med. Biol.*, vol. 66, no. 9, Apr. 2021, Art. no. 95015. [Online]. Available: https://dx.doi.org/10.1088/1361-6560/abf604

[59] K. Herweg, V. Nadig, V. Schulz, and S. Gundacker, "On the prospects of BaF2 as a fast scintillator for time-of-flight positron emission tomography systems," *IEEE Trans. Radiat. Plasma Med. Sci.*, vol. 7, no. 3, pp. 241–252, Mar. 2023. [Online]. Available: https://ieeexplore.ieee.org/document/10019596

[60] C. Bircher and Y. Shao, "Use of internal scintillator radioactivity to calibrate DOI function of a PET detector with a dual-ended-scintillator readout," *Med. Phys.*, vol. 39, no. 2, pp. 777–787, Jan. 2012. [Online]. Available: https://doi.org/10.1118/1.3676688

[61] H. T. van Dam et al., "A practical method for depth of interaction determination in monolithic scintillator PET detectors," *Phys. Med. Biol.*, vol. 56, no. 13, pp. 4135–4145, Jun. 2011. [Online]. Available: https://doi.org/10.1088/0031-9155/56/13/025